



# Investigation of Cyclic-Shear Behavior of Circular-Reinforced Concrete-Filled Steel Tubes

Hadi Kenarangi, S.M.ASCE<sup>1</sup>; and Michel Bruneau, F.ASCE<sup>2</sup>

**Abstract:** The cyclic-shear behavior of composite circular concrete-filled steel tubes (CFSTs) and reinforced concrete-filled steel tubes (RCFSTs) was experimentally and numerically investigated. Specimens with 32.39 and 40.64 cm diameters were considered, with diameter-to-thickness ratios of 51 and 64, respectively. The effects of longitudinal and transverse reinforcement were experimentally studied. The experimentally obtained strength values were compared to those from existing shear strength equations. Experimental results showed that the presence of an internal reinforcement doesn't significantly impact the shear strength of RCFSTs. All specimens exhibited some amount of ductility under cyclic shear but not necessarily to the extent that would make it a preferred ductile mechanism. The mechanics governing the shear behavior of the CFSTs were studied using validated finite-element models. It was observed that a compression strut develops in the concrete under shear deformations. This strut also contributed to the shear strength of the composite CFSTs. DOI: [10.1061/\(ASCE\)ST.1943-541X.0002598](https://doi.org/10.1061/(ASCE)ST.1943-541X.0002598). © 2020 American Society of Civil Engineers.

**Author keywords:** Concrete-filled steel tubes; Shear strength; Composite; Drilled shafts; Finite-element model; Struts; Cyclic testing.

## Introduction and Background

Reinforced concrete-filled steel tubes (RCFSTs) are structural components that consist of steel tubes filled with concrete that have a reinforcing cage inside. These members benefit mostly from the ductility of the steel tube under flexural loadings as well as the compression capacity of the reinforced concrete. Additionally, the steel casing provides confinement for the concrete (Susantha et al. 2001), and the concrete infill delays the local buckling of the steel casing by providing internal support and preventing the inward buckling, compared to a hollow steel tube; this allows effective composite action to develop (Marson and Bruneau 2004). A significant amount of experimental research has been done in the past on the flexural and axial behavior of the concrete-filled steel tubes (CFSTs) (e.g., Marson and Bruneau 2004; Leon et al. 2007; Roeder et al. 2010; Hajjar et al. 2013; Lai et al. 2014; Perea et al. 2014) and RCFSTs (Brown 2013; Moon et al. 2013; Bruneau et al. 2018).

By contrast, there is only relatively limited experimental research addressing the shear behavior of these members. Yet, the shear strength of CFST members could govern design in some instances—for example in panel zones of moment resisting frames or in drilled shafts crossing a thin liquefiable layer. In the latter case, bridge single shaft foundations constructed as reinforced concrete shafts casted in a permanent steel casing embedded in the soil sometimes span across a liquefiable soil layer sandwiched between stiffer soils above and below; in this case, seismically-induced lateral spreading of the soil above a thin liquefiable layer can

introduce severe shear loading over a short length of the RCFST shaft height (i.e., the shaft crossing the liquefiable layer is subjected to double curvature bending and resulting high shear). In this case, the shear strength of the drilled shaft can become a significant consideration in determining the final dimensions of the drilled shaft. Furthermore, for other applications beyond issues of strength, it may also be desirable to know the hysteretic behavior of such members.

Past experimental studies on the shear behavior of composite CFST and RCFST elements have, for the most part, been performed on specimens having small diameters ranging between 13.97 and 19.56 cm in single-curvature test setups subjected to monotonic loadings (Qian et al. 2007; Xu et al. 2009; Xiao et al. 2012). Roeder et al. (2016) tested larger diameter (50.8 cm diameter) RCFST and CFST shear specimens under monotonic transverse shear loading (single curvature) using a four-point bending test setup. In these tests, the shear span-to-diameter ratio ( $a/D$ ) of the specimens was set by adjusting the distance of the supports from each other to ensure a shear dominant failure.

However, a double-curvature testing condition more appropriately represents the loading and deformation states experienced by shafts spanning across liquefiable soil layers and in panel zones of moment resisting frames. A few tests have been performed using a double-curvature shear test setup (Nakahara and Tsumura 2014; Ye et al. 2016). Ye et al. (2016) tested CFSTs with an 11.94 cm diameter under monotonic loading, using a three-point bending setup with fixed support conditions at both ends, creating a double-curvature deformation. Specimens were axially loaded between 0 and 0.4 of their concrete crushing capacity ( $P_0$ ). Nakahara and Tsumura (2014) tested CFSTs with 16 and 16.5 cm diameters in a pantograph (which is a device designed to subject specimens to double curvature) and under cyclic loading. The  $a/D$  ratio of all specimens was 0.5, and the axial load ( $P$ ) varied between 0 and 0.4 times the crushing load of the concrete ( $P_0$ ).

Table 1 presents a summary of the previous experiments on the shear behavior of the composite circular CFSTs and RCFSTs. In this table,  $D/t$  is the outside diameter ( $D$ ) to the wall thickness ( $t$ ) ratio of the steel tube, and other parameters are as previously defined. Note that most specimens listed in Table 1 were of a small

<sup>1</sup>Graduate Research Assistant, Dept. of Civil, Structural, and Environmental Engineering, Univ. at Buffalo, Buffalo, NY 14260 (corresponding author). ORCID: <https://orcid.org/0000-0002-8750-7722>. Email: hadikena@buffalo.edu

<sup>2</sup>Professor, Dept. of Civil, Structural, and Environmental Engineering, Univ. at Buffalo, Buffalo, NY 14260. Email: bruneau@buffalo.edu

Note. This manuscript was submitted on February 5, 2018; approved on October 8, 2019; published online on February 27, 2020. Discussion period open until July 27, 2020; separate discussions must be submitted for individual papers. This paper is part of the *Journal of Structural Engineering*, © ASCE, ISSN 0733-9445.

**Table 1.** Existing shear tests' properties

Research	Test setup	Loading type	Outside diameter			
			( <i>D</i> ), cm	<i>D/t</i> range	<i>a/D</i> range	<i>P/P<sub>0</sub></i> range
Ye et al. (2016)	Double-curvature	Monotonic three point bending	11.94	40 and 60	0.15–0.75	0–0.73
Xiao et al. (2012)	Single-curvature	Monotonic three point bending	16.5	25–55	0.14–1.0	0–0.62
Xu et al. (2009)	Single-curvature	Monotonic three point bending	13.97	38	0.1–0.5	0
Qian et al. (2007)	Single-curvature	Monotonic three point bending	19.56	26 and 35	0.1–0.3	0–0.77
Roeder et al. (2016)	Single-curvature	Monotonic four point bending	50.8	86	0.25–1.0	0 and 0.085
Nakahara and Tsumura (2014)	Double-curvature	Cyclic pantograph	16.5	33 and 70	0.5	0–0.4

diameter and that no large diameter specimens were subjected to cyclic loading. Considering the limited existing test data, an experimental study was conducted by the authors to investigate the cyclic behavior of larger diameter CFSTs and RCFSTs to provide knowledge that can be useful for shafts spanning across thin liquefiable soil layers (when surrounding stiff soil layers induced double-curvature in the shaft), panel zones of composite moment resisting frames, and other applications in which large cyclic-shear demands may be encountered.

In this study, the results of an experimental study performed on the cyclic-shear behavior of composite CFST and RCFST members are presented. The seven shear specimens tested included a 32.39 and a 40.64 cm diameter CFST, four 32.39 cm diameter RCFSTs with various reinforcing arrangements, and a hollow 32.39 cm diameter steel tube; all were tested using a double-curvature setup and under cyclic-shear loadings. This study was performed as part of a research project investigating the contribution of the steel casing to the structural resistance of bridge single shaft foundations. These structural elements are generally made of circular reinforced concrete. In many cases, these shafts are constructed with a permanent steel tube that is placed to protect the drilled borehole in poor soil conditions. The combination of the reinforced concrete shaft encased with the steel tube forms an RCFST shaft, and it can be considered a composite member under certain conditions (Bruneau et al. 2018). The shear tests were designed to investigate the shear behavior of the composite RCFST shafts when subjected to a double-curvature shear condition that exists when the shaft spans across a thin liquefiable soil layer (as mentioned earlier). For that reason, the experimental results are compared with the shear strength predicted by equations in the AASHTO LRFD bridge design specifications (AASHTO 2014) and those from the Washington Department of Transportation's *Bridge DesignMI LRFD* (WDOT 2016). In this paper, observations from the test results and a comparison with those existing equations are reported.

## Experimental Program

Cyclic tests were conducted on seven CFST and RCFST structural members to investigate the shear strength and behavior of those

shafts. Properties of the specimens tested are presented in Table 2. In this table, *D*, *t*, and *H* are nominal outside diameter, wall thickness, and height of the shear specimen, respectively, and *a* is the shear span (i.e., *H/2* in double-curvature shear). Additionally,  $\rho_s$  is the ratio of the longitudinal reinforcement area to the cross-sectional area of the concrete infill. The average measured material properties of the steel tube and shaft concrete for each shear specimen are also presented in this table. The steel properties were obtained from steel coupons that were cut from the steel tubes, and the concrete properties were obtained from compression tests of the concrete cylinder samples. The steel tube yield strength, yield strain, and ultimate tensile strength are shown as  $F_y$ ,  $\epsilon_y$ , and  $F_u$ , respectively. Also, the uniaxial compressive strength of the concrete is shown as  $f'_c$  in this table. All specimens were made with electric resistance welded (ERW) steel pipes. All shear specimens were tested under a double-curvature setup and up to their ultimate strength and failure.

The test specimens and their relationship to each other are illustrated in Fig. 1. Specimen SH4 is a concrete-filled steel tube with a 32.39 cm outer diameter and filled with 4 ksi normal weight concrete that served as the reference specimen. To investigate the effect of longitudinal reinforcement on the shear behavior of the RCFST shafts, Specimen SH5 with  $\rho_s = 1\%$  and Specimen SH6 with  $\rho_s = 2.2\%$  were tested, and results were compared to Specimen SH4. Specimens SH7 and SH1R were tested to investigate the effect of transverse reinforcement on the shear behavior of RCFST shafts. As such, Specimens SH7 and SH1R are similar to Specimen SH5 but with No. 3 (i.e., 0.95 cm diameter) transverse spiral reinforcing bars with 10.16 and 7.62 cm pitch, respectively. Grade 60 steel (i.e.,  $F_y = 413.7$  MPa) was used for all the reinforcing. Specimen SH3 is an empty hollow structural section (HSS) tube with a 32.39 cm outer diameter, tested to provide a comparison with the shear strength of the steel tube itself. Specimen SH2 was tested to investigate the failure behavior of a CFST shaft with a larger diameter and different *D/t* and *H/D*. The dimensions and properties of the specimens were selected such that all the specimens could develop full shear yielding of the steel tube and deform and fail under a shear dominant mode prior to reaching their nominal plastic moment strength at the ends of the shear span. Additionally, the diameters and the shear spans for the specimens

**Table 2.** Shear test specimens' properties

Specimen	Outside diameter		Height ( <i>H</i> ), cm	<i>D/t</i>	<i>a/D</i>	$F_y$ , MPa	$\epsilon_y$ , $\mu$	$F_u$ , MPa	$f'_c$ , MPa	Reinforcing Gr. 60
	( <i>D</i> ), cm	Wall thickness ( <i>t</i> ), cm								
SH4	32.39	0.635	25.4	51	0.39	399.9	1,900	493.0	31.0	No Reinf.
SH5	32.39	0.635	25.4	51	0.39	399.9	1,900	493.0	31.0	Long. 6#4 ( $\rho_s = 1\%$ ) No Transverse
SH6	32.39	0.635	25.4	51	0.39	399.9	1,900	493.0	31.0	Long. 6#6 ( $\rho_s = 2.2\%$ ) No Transverse
SH7	32.39	0.635	25.4	51	0.39	399.9	1,900	493.0	31.0	Long. 6#4 Spiral #3@10.16 cm
SH1R	32.39	0.635	25.4	51	0.39	399.9	1,900	493.0	31.0	Long. 6#4 Spiral #3@7.62 cm
SH3	32.39	0.635	25.4	51	0.39	399.9	1,900	493.0	NA	No Reinf.
SH2	40.64	0.635	33.02	64	0.41	348.9	1,700	470.9	20.0	No Reinf.

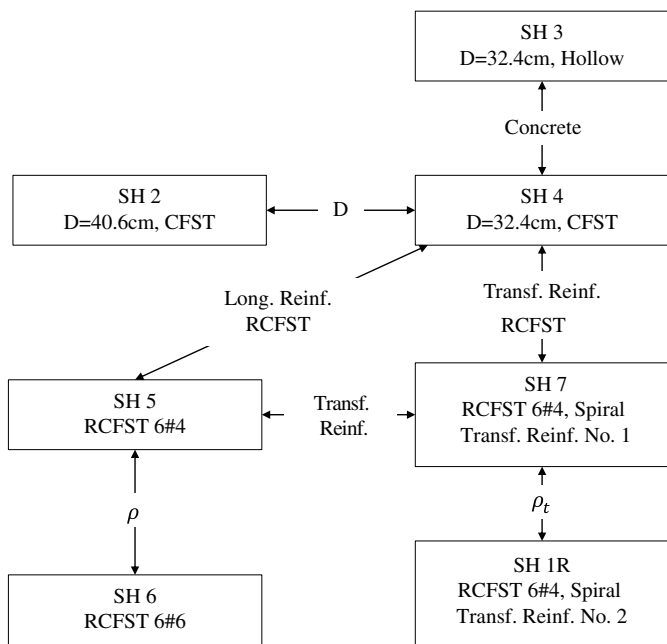


Fig. 1. Relationship of the shear test specimens to each other.

were chosen based on commonly available Grade 50 (i.e.,  $F_y = 344.7$  Mpa) ERW steel pipes on the market, the capacity limits of the test setup, and the construction costs. The process of selecting the dimensions included several finite-element analyses of different parameters, including the material properties, steel tube diameter and thickness, shear span lengths, reinforcing ratios, etc. Details of the initial analyses and design process are presented in Bruneau et al. (2018).

Specimens were tested using a pantograph device (shown in Fig. 2 without a specimen inserted), designed and constructed by Berman and Bruneau (2006). As shown in Fig. 2, in this loading device, an actuator applies a force to a loading beam (LB), such that the action line of the force passes through the midheight of a shear specimen connected to the pantograph by the top and bottom mounting plates. A cyclic load can be applied by a 440 kips (i.e., 199.6 t) capacity actuator up to displacements of  $\pm 50.8$  cm (although shear specimens can only typically resist much smaller displacements before failure). The pantograph diagonals, on the left

side, prevent the in-plane rotation of the top LB during the test, providing a double-curvature shear testing ability with pure shear at midheight of the specimen. The minimum available distance between the mounting plates of the pantograph device was 111.8 cm. To ensure a shear dominated failure in the specimens for the chosen cross-sections and material properties, the specimen length had to be on the order of 25.4 cm. Therefore, to create such a free shear span length and fit the minimum 111.8 cm specimen length required for installation into the pantograph, the strength of the specimens outside of that free span was increased by using auxiliary reinforcing steel plates. A modular test setup was designed for testing the 32.39 cm outside diameter (OD) shear specimens (labeled as 32OD shear specimens for simplicity). Based on findings from preliminary finite-element analyses and because of cost constraints, it was decided to design stiffener modules that could be bolted together with the shear specimen on the pantograph testing apparatus and then be reused for all 32OD shear specimens. Fig. 3(a) shows a schematic view of the 32OD shear specimen and the reusable stiffener modules. All the bolted connections in the modular test setup were designed as slip-critical connections. The high-strength bolts that were used for each connection were torqued to 70% of their minimum tensile strength per Section J3 of the AISC 360 (AISC 2016). Note that the modules have been sized such as to provide the desired shear span for the specimens. The exception was the 40.64 cm OD shear specimen (Specimen SH2), which was built with welded stiffeners at both ends of the shear span. Fig. 3(b) shows a schematic view of this specimen. Details regarding the dimensions, construction, and instrumentation of the specimens can be found in Bruneau et al. (2018).

The cyclic displacement loading protocol consisted of four elastic initial loadings, increasing in amplitude up to first yield strength of the specimen (i.e., force-controlled cycles). After reaching the first yield in the specimen at the end of Cycle 4, the protocol called for continued testing (in displacement-controlled cycles) by subjecting the specimen to displacement amplitudes equal to multiples of the equivalent yield displacement ( $\Delta'_y$ ), with two cycles applied at each displacement amplitude (i.e., at  $2\Delta'_y$ ,  $3\Delta'_y$ ,  $4\Delta'_y$ , etc.) until the failure of the specimen. The first and equivalent yield displacement amplitudes were chosen according to pushover results of a preliminary finite-element model of a 32OD CFST shear specimen, including the modular stiffeners and the pantograph device analyzed in LS-Dyna (LSTC 2013). Note that because the tested specimens had high lateral stiffnesses that were comparable to the lateral stiffness of the loading beam (i.e., the stiffness of the

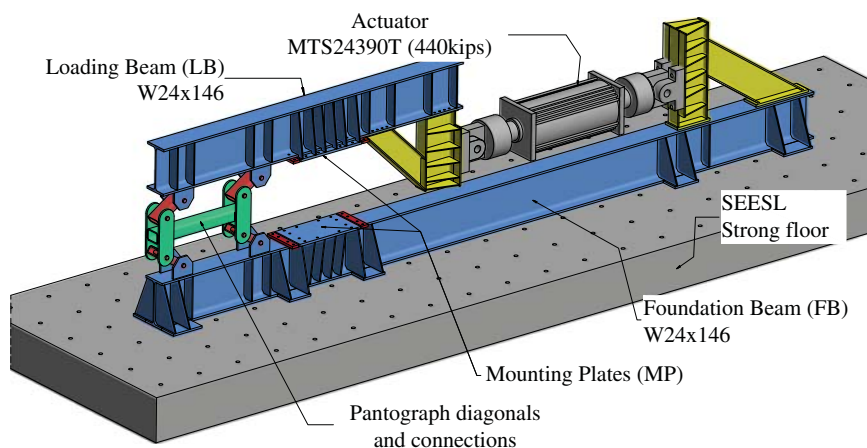
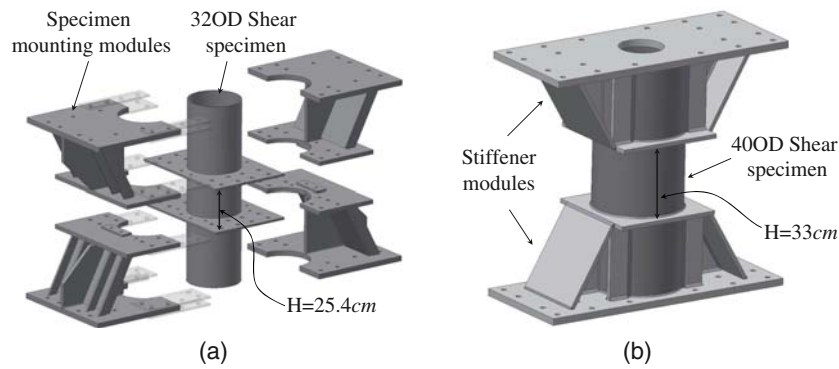


Fig. 2. Schematic view of the pantograph setup.



**Fig. 3.** (a) Schematic view of the designed modular shear test setup for 32OD shear specimens; and (b) schematic view of the designed stiffeners for Specimen SH2 (40.64 cm diameter).

members in the pantograph that transferred the load from the actuator to the specimen), all these members were included in the finite-element model to design a loading protocol that could match the experimental yield points as precisely as possible. All the specimens with similar diameters were tested under the same loading protocol. The obtained displacements of the actuator at the first yield were 6.35 and 5.08 mm for the 32OD and 40OD specimens, respectively. The calculated displacements of the actuator at the equivalent yield were 11.18 and 8.13 mm for the 32OD and 40OD specimens, respectively. Details of the finite-element model used for loading protocol design are presented later in this paper.

## Test Results

The experimentally-obtained force-displacement curves for the 32OD specimens and 40OD specimen (i.e., SH2) are shown in Figs. 4 and 5, respectively. In these figures, the horizontal axis shows the shear deformation (i.e., the lateral deformation over distance  $H$  between the stiffeners) that was recorded by string pots and a Krypton K600 LEDs camera system (SEESL 2018). Except for Specimen SH3, which was a hollow tube, some lateral slippage was observed (and heard) during the testing of the shear specimens. This slippage happened mostly (and only for certain lateral displacement ranges) at the interface of the connection between the top of the shear specimen and loading beam of the pantograph. No lateral slippage was observed at both ends of the shear span. All the specimens were instrumented by Krypton LEDs (SEESL 2018) attached to several locations on each specimen and the test setup to track deformations. The relative displacements of the LEDs from each other were checked to identify all slippage locations and their amplitudes. It was found that the largest slippages happened between the loading beam and top of the specimen. These slippages were measured using the relative displacement between LEDs mounted on the loading beam and those mounted on the top part of the specimen. The larger slippages occurred after reaching the first yield displacement and were at the order of 2.5 mm in all the concrete-filled specimens. No lateral slippage was observed at both ends of the shear span for which results are reported in this study. The complete details of the instrumentation plan can be found in Bruneau et al. (2018).

Fig. 6 shows a comparison between the force-displacement relation that is obtained using the applied displacement and shear displacement for a hollow (i.e., SH3) and a concrete-filled specimen (e.g., SH4 as a representative specimen for comparison purpose). The shear displacement was measured by subtracting values from two horizontal string pots placed at the top and bottom of the

unstiffened length of the specimens. The difference between the applied displacement and measured shear displacement is attributed to the flexibility of the stiffeners attached to the specimens as well as the pantograph itself. It was also observed that the flexibility of the pantograph device was not equal in the positive and negative directions (due to the geometry of the pantograph device). For these two reasons, the measured shear displacements were smaller than the applied displacement at the actuator and not symmetric with respect to the undeformed state.

For Specimen SH3, which was a hollow tube, diagonal local buckling started to develop after reaching the maximum experimentally achieved strength. The failure of Specimen SH3 happened by the steel tube rupturing in the middle of the shear span. Fig. 7 shows the deformation of Specimen SH3 at different loading states.

For all the other specimens, excessive diagonal deformations on the surface of the steel tube were observed after they reached their maximum strength. This deformation could be because of the failure of the diagonal compressive concrete strut that likely developed in the core of the specimen, as the lateral displacement increased in the shear span. After reaching the maximum strength, the strength of the specimens progressively decreased until cracking developed in the steel tube when a sudden loss of strength occurred. For all concrete-filled shear specimens, the failure of the specimen happened by a fracture of the steel tube on the tensile sides of the cross-section at both ends of the unstiffened span of height  $H$ . This was expected, as both ends of the shear span experience high strains caused by the interaction of bending and shear forces. Fig. 8 shows the deformed RCFST shear specimen at different loading states (Specimen SH1R is shown as a representative specimen).

Specimen SH4 (32OD CFST) reached its maximum strength at a 5% shear drift, and it failed at a 16% shear drift. The RCFST specimens (i.e., SH5, SH6, SH7, and SH1R) reached their maximum strength at an average of 6% shear drift, and their failure happened at an average shear drift of 22%. The 40.64 cm diameter CFST specimen (i.e., SH2) reached its maximum strength and failed by a steel tube fracture at 5% and 11% shear drifts, respectively. The shear drift was calculated by dividing the measured shear displacement (i.e., the measured deformation within the height of the specimen between the stiffeners) by  $H$ .

Some of the specimens were fully cut open to show the state of the infill concrete after the test. A typical result is shown in Fig. 9. As shown in the figure, the infill concrete within the shear span was pulverized into fine particles. Sheared aggregates were observed in the crushed infill concrete. Cone shaped intact parts of the concrete

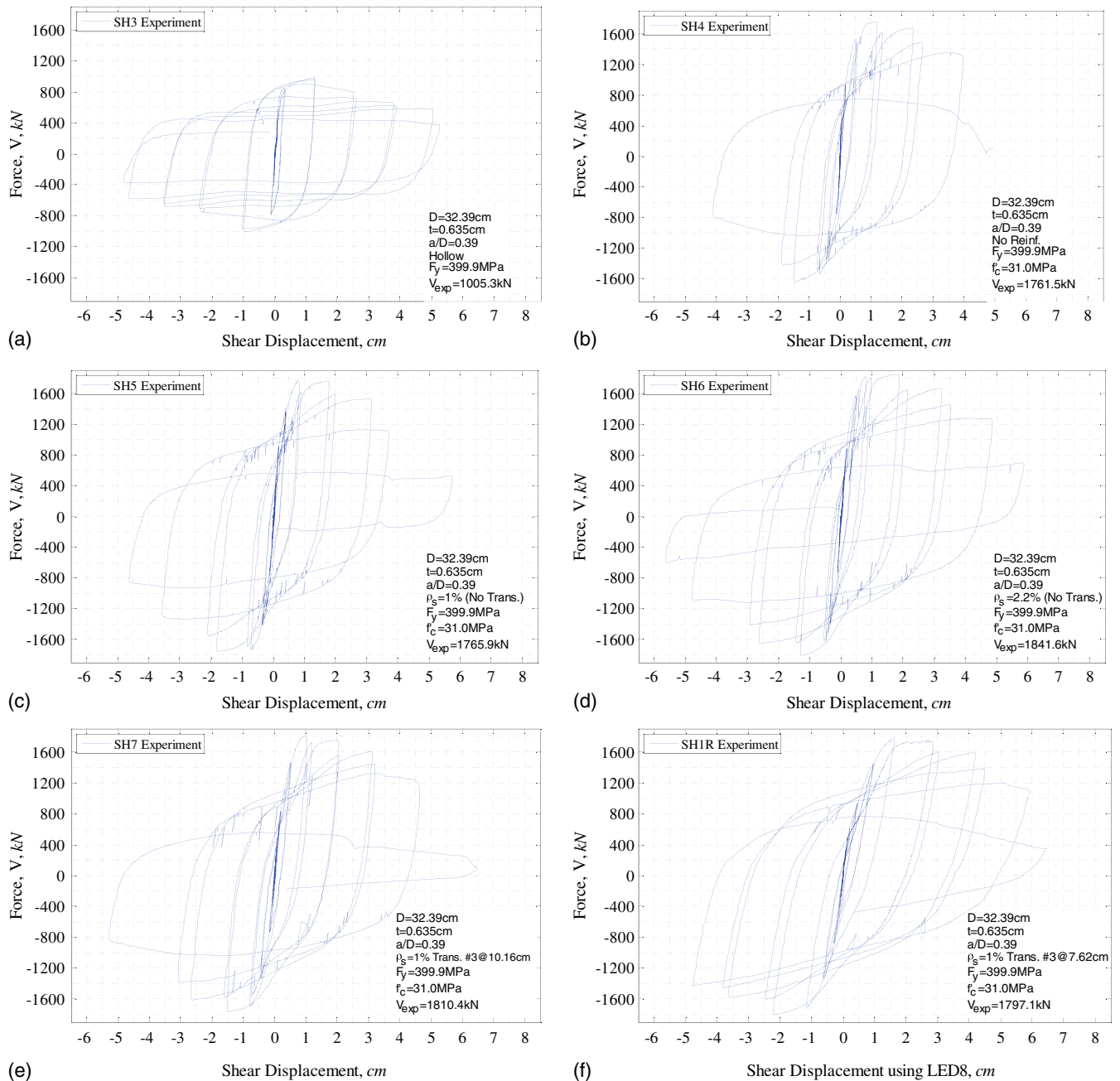


Fig. 4. Force-shear displacement curve measured from test of specimen: (a) SH3; (b) SH4; (c) SH5; (d) SH6; (e) SH7; and (f) SH1R.

core at both ends of the shear span was observed, as shown in Fig. 9. The concrete outside of the shear span was in good condition.

The experimentally-obtained shear strengths are compared in this study with the existing shear strength equations from the AASHTO LRFD bridge design specifications (AASHTO BDS) (AASHTO 2014) and those from the Washington Department of Transportation's *Bridge Design Manual LRFD* (WDOT BDM) (WDOT 2016).

Although the AASHTO BDS (AASHTO 2014) does not directly provide an equation for composite shear strength of concrete-filled steel tubes, it is assumed in this study that a practicing engineer could calculate the respective nominal shear strength of the circular steel tube and concrete section, as given by Sections 6.12.1.2.3c and 5.8.3.3, respectively, and using engineering judgment, sum them up to estimate the composite shear strength. For circular steel tubes

$$V_s = 0.5F_{cr}A_s \quad (1)$$

where  $V_s$  = shear strength of a circular steel tube; and  $F_{cr}$  = shear buckling resistance, taken as

$$F_{cr} = \left( \frac{1.60E_s}{\sqrt{\frac{L_v}{D} \left(\frac{D}{t}\right)^4}}, \frac{0.78E_s}{\left(\frac{D}{t}\right)^2} \right) \leq 0.58F_y \quad (2)$$

where  $A_s$  = area of the steel tube cross-section based on the design wall thickness;  $E_s$  = modulus of elasticity of the steel;  $F_y$  = yield strength of the steel tube;  $D$  = outside diameter of the steel tube;  $L_v$  = distance between points of maximum and 0 shear; and  $t$  = design wall thickness taken equal to 0.93 times the nominal wall thickness for ERW round HSS. For concrete

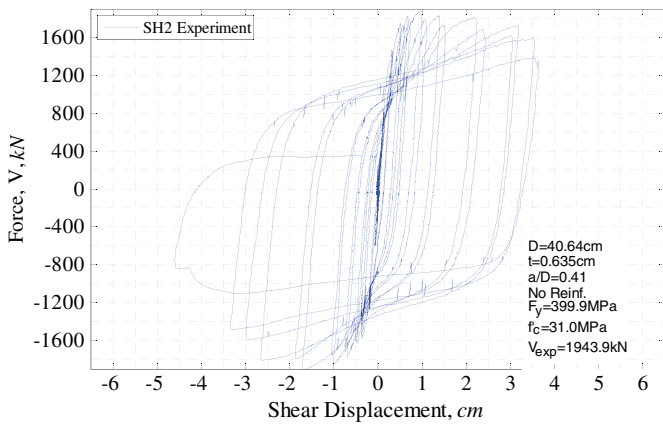


**Fig. 5.** Force-displacement curve measured from test of Specimen SH2.

$$V_c(MPa) = 0.01286\beta A_c \sqrt{f'_c(MPa)} \quad (3)$$

where  $\beta = 2.0$ ;  $f'_c$  = uniaxial compressive strength of the concrete in MPa; and  $A_c$  = area of the concrete section in  $cm^2$ . By summing these two values, the shear strength of RCFST would be

$$V_n(AASHTO) = V_s + V_c \quad (4)$$

The WSDOT BDM (WSDOT 2016), contrary to the AASHTO BDS, provides an equation for the nominal shear strength of CFST and RCFST, based on the research by Roeder et al. (2016), as

$$V_n(WSDOT) = 2V_{st} + V_{srl} + \eta V_c \quad (5)$$

where  $V_{st} = 0.6F_{yt}(0.5A_{st})$ ;  $V_{srl} = 0.6F_{yrl}(0.5A_{srl})$ ;  $\eta = 5(1 + 5\frac{P}{P_0}) \leq 10$ ;  $V_c(MPa) = 0.01286A_c \sqrt{f'_c(MPa)}$ ;  $F_{yt}$  = yield strength of the steel tube;  $A_{st}$  = cross-sectional area of the steel tube;  $F_{yrl}$  = yield strength of longitudinal bars;  $A_{srl}$  = total cross-sectional area of longitudinal bars;  $P$  = external axial load;  $P_0$  = axial capacity of the RCFST;  $A_c$  = cross-sectional area of the concrete infill in  $cm^2$ ; and  $f'_c$  = uniaxial compressive strength of the concrete infill in MPa.

Table 3 presents the maximum shear strength experimentally-obtained and the corresponding shear strengths calculated from Eqs. (4) and (5). As shown in this table, the experimentally-obtained strengths for the CFST and RCFST specimens are practically similar to each other. A maximum strength of 1,841.6 kN was obtained for Specimen SH6, which had larger diameter longitudinal bars (i.e., 6#6 with a 1.91 cm diameter) with respect to the other shear specimens, but it was observed that the presence of longitudinal bars had only a minor effect on the shear strength. For reference, the strength of the CFST (Specimen SH4, with no internal reinforcement) was 1,761.5 kN. Using 1.0% and 2.2% of a longitudinal reinforcement in Specimens SH5 and SH6, respectively, increases the strength to 1,765.9 and 1,841.6 kN, respectively. Comparing the shear strengths of Specimens SH7 and SH1R with that of Specimen SH5 shows that the existence of a spiral reinforcement does not have a significant effect on the shear strength either, as it only increases the shear strength by 44.5 and 31.1 kN for Specimens SH7 and SH1R, respectively, compared to that of SH5.

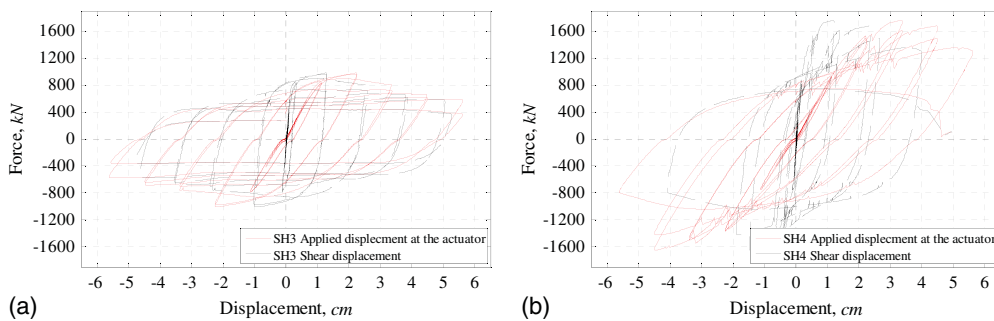


**Fig. 6.** Force-displacement relations comparison for applied displacement and measured shear span displacement.

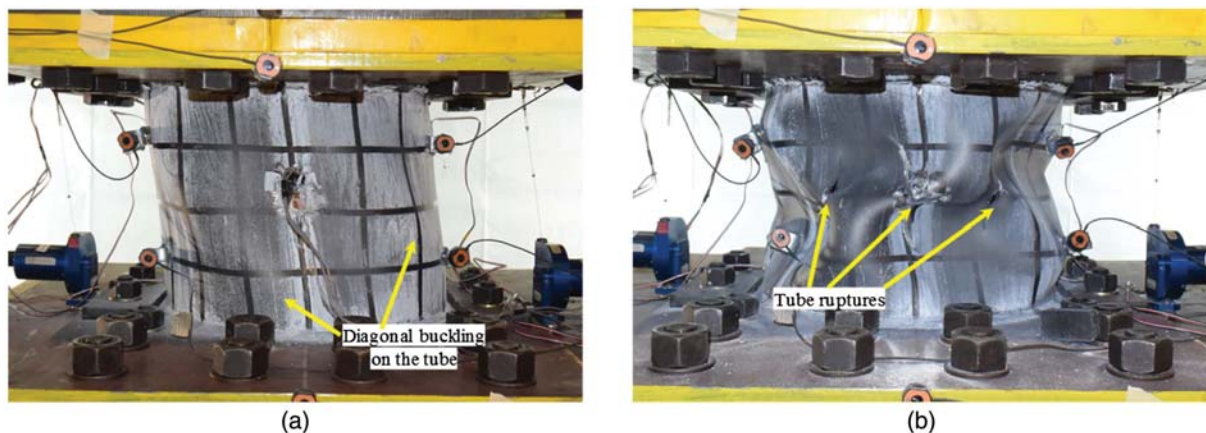


**Fig. 7.** Deformation of SH3 shear specimen (hollow tube): (a) after reaching maximum strength; and (b) specimen failure.



**Fig. 8.** Deformation of RCFST shear specimen (SH1R shaft 6#4, #3@7.62 cm): (a) after reaching maximum strength; and (b) specimen failure.



**Fig. 9.** Infill concrete state after shear test.

**Table 3.** Comparison of experimentally-obtained strengths and existing shear strength equations

Specimen	Specimen strength ( $V_{exp}$ ), kN (experimental)	AASHTO BDS (AASHTO 2014) ( $V_{n(AASHTO)}$ ), kN	WSDOT BDM (WDOT 2016) ( $V_{n(WSDOT)}$ ), kN	$\hat{V}_A = \frac{V_{exp}}{V_{n(AASHTO)}}$	$\hat{V}_W = \frac{V_{exp}}{V_{n(WSDOT)}}$
SH4 (32OD CFST)	1,761.5	756.2	1,588.0	2.33	1.11
SH5 (32OD RCFST 6#4, $\rho_s = 1\%$ )	1,765.9	756.2	1,685.9	2.34	1.05
SH6 (32OD RCFST 6#6, $\rho_s = 2.2\%$ )	1,841.6	756.2	1,801.5	2.44	1.02
SH7 (32OD RCFST 6#4, #3@10.16)	1,810.4	756.2	1,685.9	2.39	1.07
SH1R (32OD RCFST 6#4, #3@7.62)	1,797.1	756.2	1,685.9	2.38	1.07
SH3 (32OD hollow)	1,005.3	685.0	1,414.5	1.47	NA
SH2 (40OD CFST)	1,943.9	840.7	1,783.7	2.31	1.09

Comparing the experimental backbone curves of Specimen SH3 (hollow) and Specimen SH4 (CFST) shows that the initial stiffness of the shear specimens is similar to each other. However, the maximum shear strength of Specimen SH3 was 57.1% of that obtained for Specimen SH4, and the ultimate behavior was most different (as previously described).

The experimental backbone curves of all concrete-filled 32OD shear specimens (i.e., CFTS and RCFSTs) are compared with the existing shear strength equations in AASHTO BDS (AASHTO 2014) and WSDOT BDM (WDOT 2016) in Fig. 10(a). As shown in this figure, the AASHTO BDS (AASHTO 2014) equations, used

as previously described, give conservative values for the shear strength of the tested CFST and RCFSTs. The shear strength calculated by the WSDOT BDM (WDOT 2016) equation is closer to the experimentally-obtained shear strength values.

Fig. 10(b) shows the experimental backbone curve of Specimen SH3 (32OD hollow) and the shear strength calculated by the AASHTO BDS (AASHTO 2014) using Eq. (1), which is basically the equation for shear strength of a hollow circular steel tube. As shown in the figure, the experimentally-obtained shear strength for a circular HSS tube is greater than that estimated by AASHTO BDS (AASHTO 2014), which is conservative. Note that a design

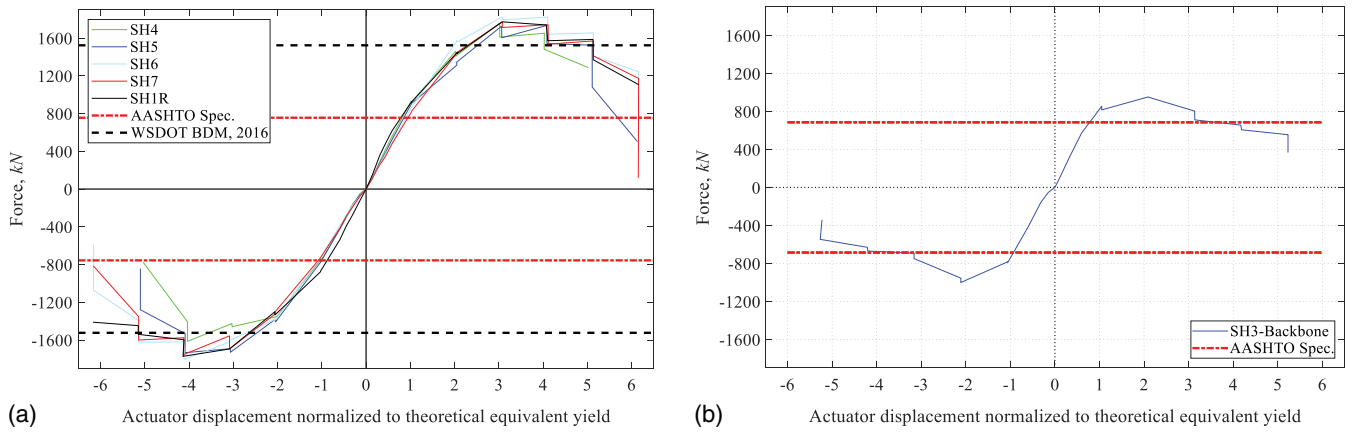


**Fig. 10.** (a) Comparison of backbone curves of tested 32OD CFST and RCFSTs with existing shear strength equations; and (b) comparison of backbone curve of Specimen SH3 (32OD hollow) and the shear strength calculated by AASHTO BDS (AASHTO 2014).

equation for CFSTs should provide conservative strength when extrapolated across the entire continuum of relative steel and concrete strengths, ranging from steel dominant to concrete dominant CFSTs. The hollow tube case is at the extreme limit of that continuum. It is recognized in this study that the shear strength of hollow tubes (or presumably tubes infilled with materials significantly weaker/softer than the concretes used in past experiments that cannot contribute to the total shear resistance) should not be calculated using the WSDOT BDM (WDOT 2016) equation using a zero value for the compressive strength of the concrete. This will result in unconservative shear strength values.

### Numerical Modeling of the Shear Specimens

The LS-Dyna (LSTC 2013) model of the shear specimen and test setup is schematically shown in Fig. 11. To include the effects of the flexibility of the pantograph device on the stiffness of the shear specimen and the amplitude of the applied lateral displacements, the shear specimen and the upper part of the pantograph were modeled, including the stiffener modules, loading beam, and pantograph diagonals. A half-finite-element model was built taking advantage of the symmetry existing in the test setup.

A Winfrith concrete material model with constant stress solid elements was used for the concrete part. A bilinear elastoplastic material with 1% strain hardening was used for the modeling of

the steel parts. Pretensioning forces of the bolts were applied by shortening the length of the bolts at the beginning of the analyses using temperature loading (and defining a thermal expansion coefficient along the axis of the bolt). This pretension force of the bolts was tuned to 70% of their yield strength. The thermal expansion coefficient for each bolt depended on the total thickness of the bolted plates in the connection and the diameter of the bolt and was determined by a trial-and-error procedure. Tie contact was used to model the weld connections in the model. The moving parts of the pantograph (on the left side of Fig. 11) were modeled as rigid parts, and the pinned joints between these parts were modeled using revolute joint constraints. This finite-element model was used prior to the shear tests for assessing the adequacy of the test setup and to design the cyclic loading protocol. Complete details of the developed finite-element model can be found in Bruneau et al. (2018). Specified material properties were used for pretest finite-element analyses. For posttest analyses, the average material properties presented in Table 2 were used for the steel tube and concrete. All other steel plates were modeled assuming 344.7 MPa for their yield strength (i.e., a nominal yield strength), and bolts were modeled assuming 896.3 MPa for their yield strength (i.e., a nominal yield strength). To reduce the runtime of the finite-element analyses, the repeated cycles at each nonlinear displacement amplitude in the test loading protocol were not considered in the cyclic displacement history applied to the finite-element model. The self-weight of the specimen and test setup were not considered in the simulations because they were small enough to have no effect on the results. Note that, as mentioned earlier, the test results for the RCFST shafts were generally similar to those for the CFST shear specimen (i.e., Specimen SH4). For this reason, finite-element analyses are shown only for the CFST shear specimen.

Fig. 12 shows the finite-element results for Specimen SH4 (the 32.39 cm diameter CFST). In this figure, the numerically-obtained hysteresis curves are compared with the experimental results, with the horizontal axis displaying actuator and shear displacements in Figs. 12(a and b), respectively. As shown in Fig. 12(a), the initial global stiffness of the test setup was well captured by the finite-element model. Also, as shown in Fig. 12(b), the initial stiffness of the specimen in the shear span was also well matched with the experimentally-obtained results. No failure criteria were defined for the concrete and steel materials, and, therefore, no failure is exhibited by the finite-element analyses. In fact, in the finite-element analyses, the concrete's strength kept increasing progressively at larger drifts. This increase was consistent with the

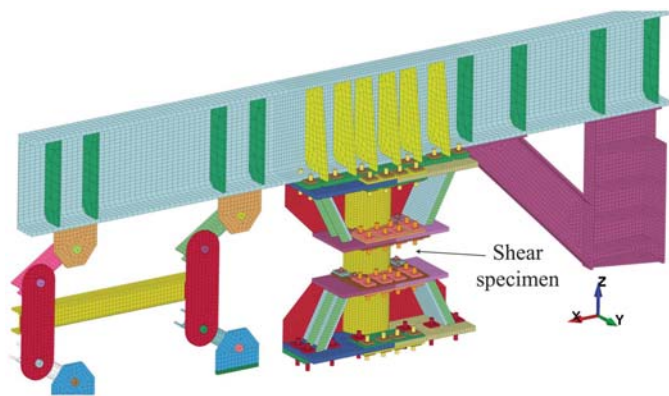


**Fig. 11.** Scheme of the developed LS-Dyna finite-element model for the shear tests.

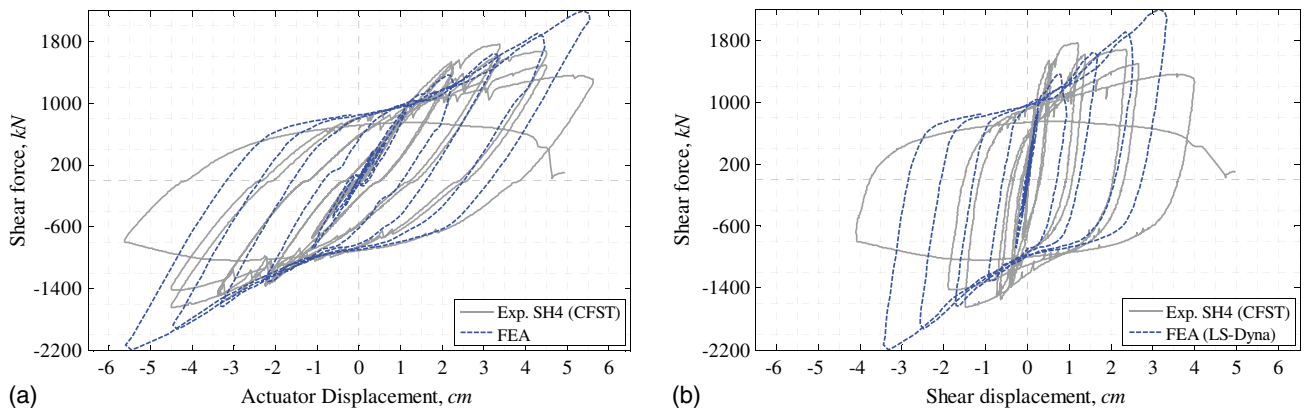


**Fig. 12.** Finite-element analysis and experimental results comparison for Specimen SH4; showing (a) actuator displacement; and (b) shear displacement, on the X-axis.

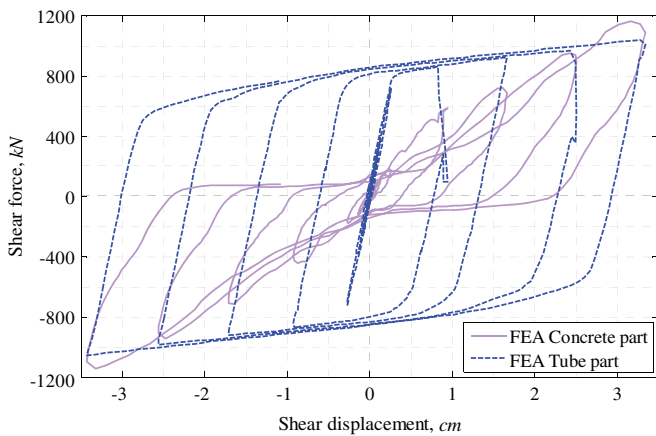


**Fig. 13.** Shear force carried by the steel tube and the concrete part of Specimen SH4.

development of a diagonal compression strut in the concrete. This behavior is observed in Fig. 13, which shows the shear force respectively carried by the steel tube and the concrete of Specimen SH4. The shear contributions of the steel tube and the concrete were calculated by integration of the shear forces on the cross-section of the steel tube and concrete individually. The summation of these contributions is equal to the total shear carried by the composite cross-section.

Fig. 14 shows Von-Mises stress contours on the surface of the steel tube at the point where the steel tube yields (i.e., the first yield point of the steel tube according to the finite-element results) and at the point where the maximum experimental strength was obtained during the test. As shown in these figures, the yielding of the steel tube started from the center of the cross-section near the midspan of the specimen and propagated toward the unstiffened span ends at the larger displacements.

Fig. 15 shows principal stress vectors on the concrete at the middle of the cross-section. The compression strut that developed in the concrete as a result of shear deflection can be seen in this figure. The increase in the shear strength of the concrete shown in Fig. 13 is because of the development of a diagonal compression strut. The length of shear span affects the strength of this strut. Fig. 16 shows Von-Mises stress contours on the surface of the steel tube at the maximum positive displacement.

The shear force carried by each part that is shown in Fig. 13 is compared to the shear strength values that were calculated using the AASHTO BDS (AASHTO 2014) and the WSDOT BDM (WDOT 2016) equations in Fig. 17. As shown in Fig. 17(a), the shear strength of the steel tube given by the AASHTO BDS (AASHTO 2014), which is, in fact, equal to the shear yield strength of a hollow circular steel tube, matches the first yield strength obtained from finite-element analysis. Also, it is observed that the shear strength given by the AASHTO BDS (AASHTO 2014) for the concrete part does not consider the effect of the compression strut discussed previously and only considers the material based (cross-section) shear strength of the concrete. This can be seen by comparing the shear strength values given by AASHTO BDS (AASHTO 2014) with the shear force at the concrete at the unloading branches in Fig. 17(a). As shown in Fig. 17(b), the shear strength of the steel tube given by WSDOT BDM (WDOT 2016) is about 2 times the shear force in the steel tube at the first yield point obtained from the finite-element analysis. The strength of the steel tube given by WSDOT BDM (WDOT 2016), which is two times the shear yield strength of the steel tube ( $V_{st}$ ) as calculated in Eq. (5) is 1.64 times the plastic shear strength of a hollow steel tube that is calculated by integrating the shear yield stresses tangent to the surface of the steel tube over the cross-section (i.e.,  $V_{pst} = 1.22V_{st}$ ). As shown in Fig. 17(b) it was observed from the finite-element analysis that the contribution of the steel tube considering the strain hardening effects is much less than the value given by WSDOT BDM (WDOT 2016).

## Conclusion

Results obtained from the cyclic testing and numerical analysis performed on seven RCFSTs subjected to shear under double-curvature flexural loading made it possible to observe the following:

- The inclusion of longitudinal reinforcement did not have a significant effect on the strength of the RCFST shafts. The maximum experimentally-obtained shear strength increased by only 0.25% for RCFSTs having 1% longitudinal reinforcement, and it increased by 4% for RCFSTs having 2.2% reinforcement. The inclusion of longitudinal reinforcement had a minor effect in delaying the failure of the specimens.
- The inclusion of a transverse reinforcement also did not have a significant effect on the strength and ductility of the RCFST shafts.

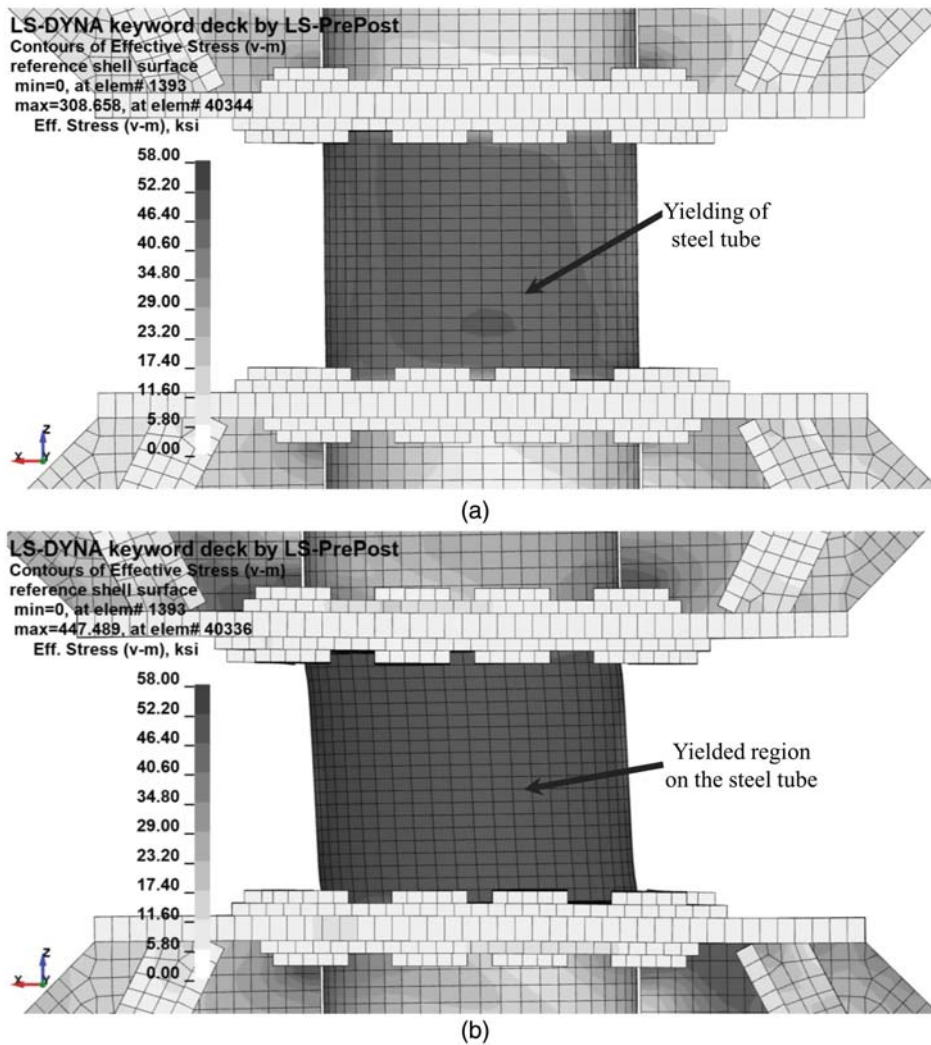


**Fig. 14.** Von-Mises stress contours on the steel tube of Specimen SH4 at: (a) first yield point; and (b) maximum experimental strength point.

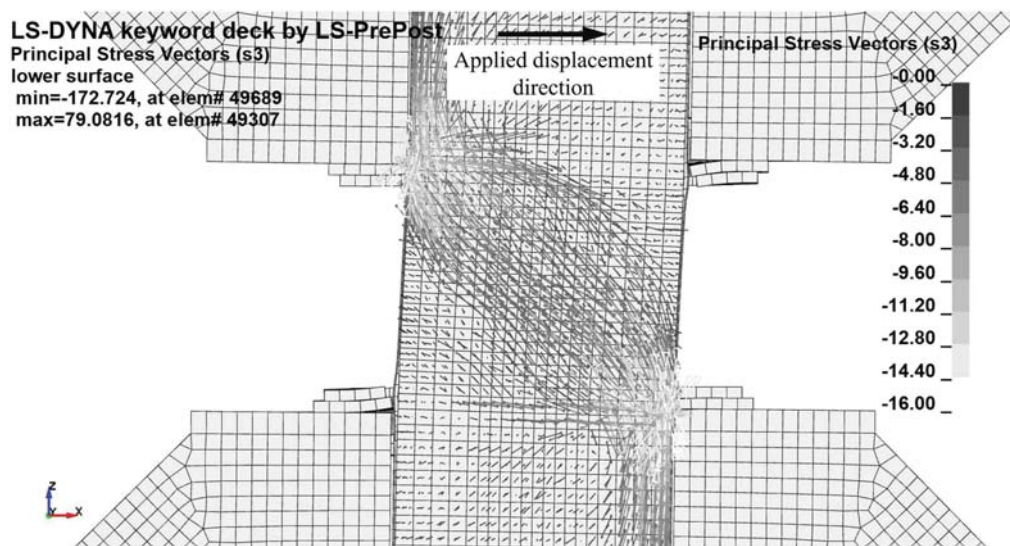


**Fig. 15.** Principal stress vectors on the concrete at the middle of the cross-section of Specimen SH4 at the maximum experimental strength point.

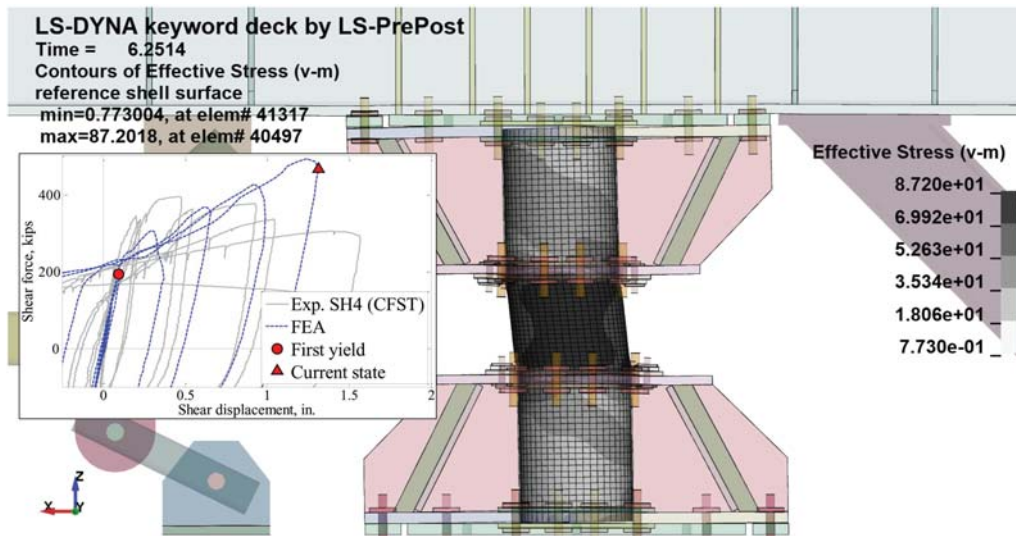


Fig. 16. Von-Mises stress contours on the steel tube of Specimen SH4 at the maximum positive drift.

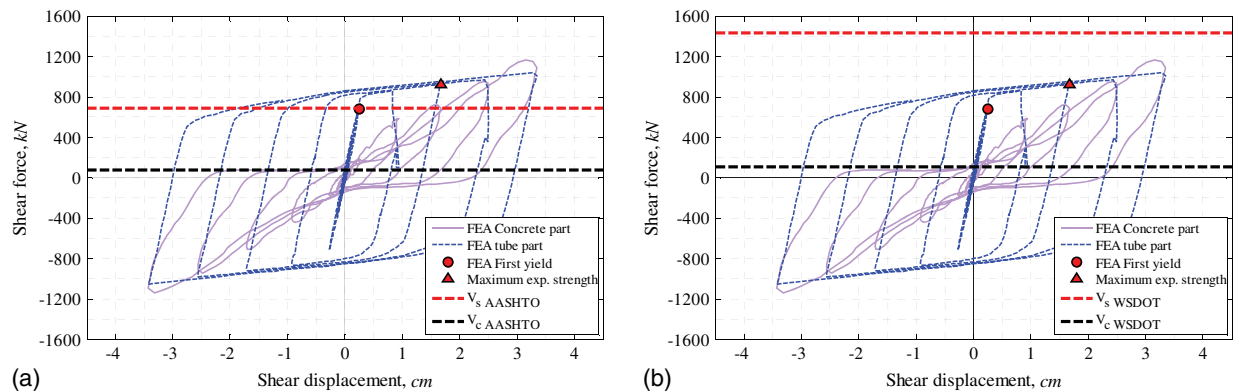


Fig. 17. Comparison of component shear forces with: (a) AASHTO BDS (AASHTO 2014); and (b) WSDOT BDM (WDOT 2016).

- The shear strength obtained by summing the individual shear strengths given by the equations in the AASHTO guide specifications for LRFD seismic bridge design (AASHTO 2014) for a hollow steel tube and concrete section underestimated the strength of the CFST and RCFST shafts by a factor of more than 2.0. The experimentally-obtained shear strength of the hollow steel tube was 1.47 times the strength calculated by the AASHTO equations.
- The composite shear strength equation for CFST provided by the Washington Department of Transportation's *Bridge Design Manual LRFD* (WDOT 2016) gave results closer to the experimentally-obtained shear strength values. However, it overestimated the contribution of the steel tube to the total strength (and should not be used for nonfilled steel tubes) and underestimated the contribution of the concrete.
- All specimens exhibited some amount of ductility under cyclic shear, but it is unknown what factors would be sufficient to make it a preferred ductile mechanism (future research could investigate this issue). The maximum strength of the 32.39 cm diameter RCFST specimens, on average, was reached at 6% shear drifts, while the maximum strength of the 32.39 cm diameter CFST shaft was reached at a 5% shear drift. Failure happened at average shear drifts of 22% and 16% for the 32.39 cm diameter RCFST and CFST, respectively. For the 40.64 cm

diameter CFST specimen, the maximum strength was reached at the 5% shear drift, and failure happened at the 11% shear drift.

- As shown by finite-element analyses results, the yielding of the steel tube started from the center of the cross-section and propagated toward the shear span ends at the larger displacements. A compression strut developed in the concrete as a result of shear deflection. The developed strut had a major contribution to the shear strength of concrete-filled tubes.

## Acknowledgments

This work was sponsored by the AASHTO in cooperation with the Federal Highway Administration (FHWA). It was conducted in the National Cooperative Highway Research Program (NCHRP), which is administrated by the Transportation Research Board (TRB) of the National Academies of Sciences, Engineering, and Medicine, under the research project NCHRP 12-93. The authors thank the NCHRP 12-93 Program Officer and the other members of the Project's Advisory Panel. However, any opinions, findings, conclusions, and recommendations presented in this report are those of the writers and do not necessarily reflect acceptance by or the views of the National Academy, the TRB, the FHWA, or AASHTO.

## References

- AASHTO. 2014. *AASHTO LRFD bridge design specifications, customary U.S. units, 7th edition, with 2015 interim revisions*. Washington, DC: AASHTO.
- AISC. 2016. *Specification for structural steel buildings*. AISC 360. Chicago: AISC.
- Berman, J. W., and M. Bruneau. 2006. *Further development of tubular eccentrically braced frame links for the seismic retrofit of braced steel truss bridge piers*. Buffalo, NY: Multidisciplinary Center for Earthquake Engineering Research.
- Brown, N. K. 2013. "Strain limits for concrete filled steel tubes in AASHTO seismic provisions." M.Sc. thesis, Dept. of Civil, Construction, and Environmental Engineering, North Carolina State Univ.
- Bruneau, M., H. Kenarangi, and T. P. Murphy. 2018. *NCHRP research report 872 contribution of steel casing to single shaft foundation structural resistance*. Washington, DC: Transportation Research Board.
- Hajjar, J. F., B. C. Gourley, C. Tort, M. D. Denavit, and P. H. Schiller. 2013. "Steel-concrete composite structural systems." Accessed January 23, 2018. <http://www.northeastern.edu/compositesystems>.
- Lai, Z., A. H. Varma, and K. Zhang. 2014. "Noncompact and slender rectangular CFT members: Experimental database, analysis, and design." *J. Constr. Steel Res.* 101 (Oct): 455–468. <https://doi.org/10.1016/j.jcsr.2014.06.004>.
- Leon, R. T., D. K. Kim, and J. F. Hajjar. 2007. "Limit state response of composite columns and beam-columns. Part I: Formulation of design provisions for the 2005 AISC specification." *Eng. J.* 44 (1): 341–358.
- LSTC (Livermore Software Technology Corporation). 2013. *LS-DYNA keyword user's manual version R7.0*. Livermore, CA: LSTC.
- Marson, J., and M. Bruneau. 2004. "Cyclic testing of concrete-filled circular steel bridge piers having encased fixed-based detail." *J. Bridge Eng.* 9 (1): 14–23. [https://doi.org/10.1061/\(ASCE\)1084-0702\(2004\)9:1\(14\)](https://doi.org/10.1061/(ASCE)1084-0702(2004)9:1(14)).
- Moon, J., D. E. Lehman, C. W. Roeder, and H. E. Lee. 2013. "Strength of circular concrete-filled tubes with and without internal reinforcement under combined loading." *J. Struct. Eng.* 139 (12): 04013012. [https://doi.org/10.1061/\(ASCE\)ST.1943-541X.0000788](https://doi.org/10.1061/(ASCE)ST.1943-541X.0000788).
- Nakahara, H., and R. Tsumura. 2014. "Experimental study on shearing behavior of circular CFT short column." *J. Struct. Constr. Eng.* 79 (703): 1385–1393. <https://doi.org/10.3130/aijs.79.1385>.
- Perea, T., R. T. Leon, J. F. Hajjar, and M. D. Denavit. 2014. "Full-scale tests of slender concrete-filled tubes: Interaction behavior." *J. Struct. Eng.* 140 (9): 04014054. [https://doi.org/10.1061/\(ASCE\)ST.1943-541X.0000949](https://doi.org/10.1061/(ASCE)ST.1943-541X.0000949).
- Qian, J., Y. Cui, and X. Fang. 2007. "Shear strength tests of concrete filled steel tube columns." *Tumu Gongcheng Xuebao (China Civ. Eng. J.)* 40 (5): 1–9.
- Roeder, C., D. Lehman, and E. Bishop. 2010. "Strength and stiffness of circular concrete-filled tubes." *J. Struct. Eng.* 136 (12): 1545–1553. [https://doi.org/10.1061/\(ASCE\)ST.1943-541X.0000263](https://doi.org/10.1061/(ASCE)ST.1943-541X.0000263).
- Roeder, C., D. Lehman, and A. Maki. 2016. *Shear design expressions for concrete filled steel tube and reinforced concrete filled tube components*, 142. Olympia, WA: Washington State Department of Transportation.
- SEESL (University at Buffalo Structural and Earthquake Engineering Simulation Laboratory). 2018. "SEESL lab manual." Accessed February 5, 2018. <http://nees.buffalo.edu/docs/labmanual/SEESLLabManual.pdf>.
- Susantha, K., H. Ge, and T. Usami. 2001. "Uniaxial stress-strain relationship of concrete confined by various shaped steel tubes." *Eng. Struct.* 23 (10): 1331–1347. [https://doi.org/10.1016/S0141-0296\(01\)00020-7](https://doi.org/10.1016/S0141-0296(01)00020-7).
- WDOT (Washington Department of Transportation). 2016. *Bridge design manual LRFD*. Olympia, WA: WDOT.
- Xiao, C., S. Cai, T. Chen, and C. Xu. 2012. "Experimental study on shear capacity of circular concrete filled steel tubes." *Steel Compos. Struct.* 13 (5): 437–449. <https://doi.org/10.12989/scs.2012.13.5.437>.
- Xu, C., L. Haixiao, and H. Chengkui. 2009. "Experimental study on shear resistance of self-stressing concrete filled circular steel tubes." *J. Constr. Steel Res.* 65 (4): 801–807. <https://doi.org/10.1016/j.jcsr.2008.12.004>.
- Ye, Y., L. H. Han, Z. Tao, and S. L. Guo. 2016. "Experimental behaviour of concrete-filled steel tubular members under lateral shear loads." *J. Constr. Steel Res.* 122 (Jul): 226–237. <https://doi.org/10.1016/j.jcsr.2016.03.012>.